Anisotropic valence→core x-ray fluorescence from a $[Rh(en)_3][Mn(N)(CN)_5]\cdot H_2O$ single crystal: Experimental results and density functional calculations

U. Bergmann
Department of Applied Science, University of California, Davis, California 95616 and Physical Biosciences Division, Lawrence Berkeley National Laboratory, Berkeley, California 94720

J. Bendix
Division of Chemistry and Chemical Engineering, California Institute of Technology, Pasadena, California 91125

P. Glatzel
Department of Applied Science, University of California, Davis, California 95616

H. B. Gray
Division of Chemistry and Chemical Engineering, California Institute of Technology, Pasadena, California 91125

S. P. Cramer[a)]
Department of Applied Science, University of California, Davis, California 95616 and Physical Biosciences Division, Lawrence Berkeley National Laboratory, Berkeley, California 94720

(Received 21 June 2001; accepted 28 September 2001)

High resolution x-ray fluorescence spectra have been recorded for emission in different directions from a single crystal of the compound $[Rh(en)_3][Mn(N)(CN)_5]\cdot H_2O$. The spectra are interpreted by comparison with density functional theory (DFT) electronic structure calculations. The $K\beta''$ line, which is strongly polarized along the Mn–N axis, can be viewed as an $N(2s)\rightarrow Mn(1s)$ transition, and the angular dependence is understood within the dipole approximation. The so-called $K\beta_{2,5}$ region has numerous contributions but is dominated by $Mn(4p)$ and $C(2s)\rightarrow Mn(1s)$ transitions. Transition energy splittings are found in agreement with those of calculated occupied molecular orbitals to within 1 eV. Computed relative transition probabilities reproduce experimentally observed trends. © *2002 American Institute of Physics.* [DOI: 10.1063/1.1419062]

I. INTRODUCTION

X-ray fluorescence (XRF) is a century-old technique that has been revitalized by continuing development of brighter synchrotron radiation sources. Because the energies and relative intensities of x-ray emission lines are nearly invariant for a given element, XRF is used routinely as an analytical tool for elemental analysis and particle characterization.[1] However, chemical effects on XRF have been known for many years,[2] and they have been often used as a probe of chemical bonding.[3] With modern high intensity synchrotron radiation sources and improved analyzer instrumentation,[4] spectra can now be obtained on dilute systems such as metalloproteins.[5]

The largest chemical effects involve valence→core x-ray transitions, which carry information about the occupancy and symmetry of the orbitals involved in chemical bonding. For transition metal complexes, the 1*s* orbital is tightly localized on the metal center, and a common assumption is that the fluorescence intensity reflects the amount of metal *p* character in a particular orbital. In this work we use density functional theory (DFT) calculations to interpret the valence→core x-ray emission spectra of a $[Rh(en)_3][Mn(N)(CN)_5]\cdot H_2O$ single crystal.

II. EXPERIMENT

A. Samples

The compound $[Rh(en)_3][Mn(N)(CN)_5]\cdot H_2O$ was prepared by the literature method.[6] This material forms pencil shaped crystals in the hexagonal space group $P63$.[6,7] The short (1.5 Å) Mn–N triple bond is oriented close to the long C_6 crystal axis—all of the Mn–N vectors are within 9° of C_6.

B. Data collection and processing

The experiment was performed on beamline 10-2 at the Stanford Synchrotron Radiation Laboratory (SSRL) using a Si(1,1,1) monochromator and a focused beam. The x-ray energy was tuned to 9.1 keV for excitation, well above the Mn 1*s* binding energy (6.54 keV). Fluorescence spectra were recorded with a high-resolution multicrystal spectrometer[4] and a liquid nitrogen cooled germanium detector.

For measurements of the angular dependence of the emission, analyzer crystals were used in pairs. This was a compromise between angular resolution and collection effi-

[a)]Author to whom correspondence should be addressed.

ciency. The angular acceptance per crystal analyzer is $\pm 3°$ and the analyzers were separated by 8°–10° resulting in a total angular spread of $\sim \pm 10°$. All eight analyzers were employed to study the polycrystalline sample. At each angle, both the valence→core and the main $K\beta$ region were recorded. Sample damage due to photoreduction results in a shift of the $K\beta_{1,3}$ main peak, and only unaffected spectra were included in the data analysis.

To quantify the $K\beta''$ transition intensities, the spectra were first normalized to a constant value for the integrated $K\beta_{1,3}$ region. Then, a smooth background corresponding to the tails of the $K\beta_{1,3}$ and $K\beta_{2,5}$ transitions was subtracted from the normalized spectra.

C. Density functional calculations

DFT calculations were performed with the Amsterdam Density Functional (ADF) program suite version 1999.[8–11] Slater-type orbital basis sets of triple-ζ quality were employed with polarization functions on the ligand atoms ($3d$ for C and N) and additional valence p orbitals on the metal atoms (ADF basis set IV). Nonlocal and local calculations differed little. The exchange functional proposed by Becke[12] and the correlation functional due to Perdew[13,14] were used. All charge and spin densities were based on Mulliken analyses.[15] Transition energies were calculated using Slater's transition state method.[16]

The contributions of different orbitals to the $K\beta_{1,3}$, $K\beta_{2,5}$, and $K\beta''$ transition intensities were evaluated by dumping the TAPE21 file from the ADF program, converting it to a text file using the ''dmpkf'' program, and extracting the coefficients of the simple Slater-type orbitals in the pertinent eigenfunctions by hand. The dipole matrix elements $\langle \mathrm{Mn}\, 1s|\mathbf{r}|\phi\rangle$, where ϕ is the atomic orbital, were then evaluated numerically using the NIntegrate.

III. RESULTS AND DISCUSSION

The overall $K\beta$ spectrum for polycrystalline $[\mathrm{Rh(en)_3}][\mathrm{Mn(N)(CN)_5}]\cdot \mathrm{H_2O}$ is shown in Fig. 1, along with the structure of the anion and its orientation within the crystal. For comparison, the spectra of MnO_2 and Mn metal are also shown. The core→core region of the spectra contains a main $K\beta_{1,3}$ peak that is primarily a $3p \rightarrow 1s$ transition, along with a low energy tail that has been labeled $K\beta'$. The difference in energy is reasonably well explained by a $3p-3d$ final state exchange interaction.[17] The strongest valence→core features are labeled $K\beta_{2,5}$ lines. These transitions involve the highest energy molecular orbitals with Mn $3d$, $4s$, and $4p$ character as well as carbon and nitrogen $2s$ and $2p$ character. At lower energy, $K\beta''$ transitions are seen in the compounds (but not for the metal). These features, also known as ''crossover'' peaks, have been assigned as ligand $2s \rightarrow$ metal $1s$ transitions, and they reflect the ligand $2s$ binding energies.[18] However, the origin of the transition intensity is not completely settled.

To better understand the electronic origin of these features, we recorded emission spectra of the emission in different directions from a single crystal of $[\mathrm{Rh(en)_3}][\mathrm{Mn(N)(CN)_5}]\cdot \mathrm{H_2O}$ (Fig. 2). As shown in Fig. 3,

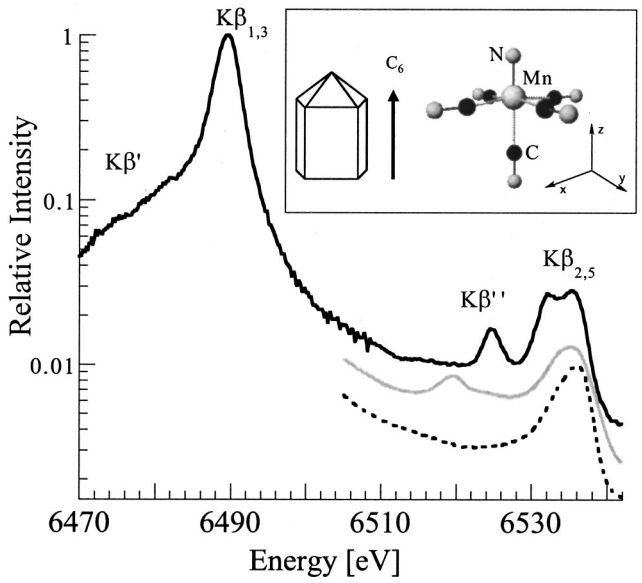

FIG. 1. $K\beta$ spectrum of polycrystalline $[\mathrm{Rh(en)_3}][\mathrm{Mn(N)(CN)_5}]\cdot \mathrm{H_2O}$. For comparison the valence regions of MnO_2 (gray) and Mn-metal (dashed) are shown. Note the absence of $K\beta''$ in the metal spectrum and the ~6 eV shift reflecting the energy of the O $2s$ level in the MnO_2 spectrum. Inset: C_6 crystal shape and local Mn structure of $[\mathrm{Rh(en)_3}][\mathrm{Mn(N)(CN)_5}]\cdot \mathrm{H_2O}$.

we find that the intensity of the $K\beta''$ line is strongly dependent on the emission direction. This ''crossover'' peak is strongest at an emission angle of 90° with respect to the Mn≡N axis, and it gradually decreases until it is essentially invisible at 8°. The intensity exhibits the $\sin^2\theta$ dependence expected for a dipole transition, and the value measured for the polycrystalline sample agrees reasonably well with that predicted for the ''magic angle'' of 54.7° (Fig. 3).

We have used DFT calculations to quantitatively interpret these spectra. We began by calculating the ground state properties of $[\mathrm{Mn(N)(CN)_5}]^{3-}$ with the local density approximation (LDA) as well as with gradient corrected (GC) functionals. The results for the optimized geometries and for

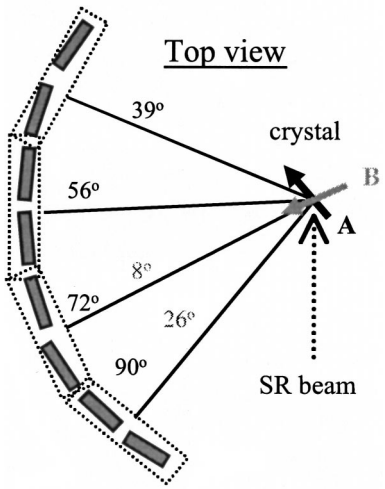

FIG. 2. Experimental setup for the single crystal experiments. Two analyzers (dotted line) were used for measurements at a given angle. Arrows indicate the crystal C_6 axis (short Mn–N bond) in the two experimental geometries A and B (grey).

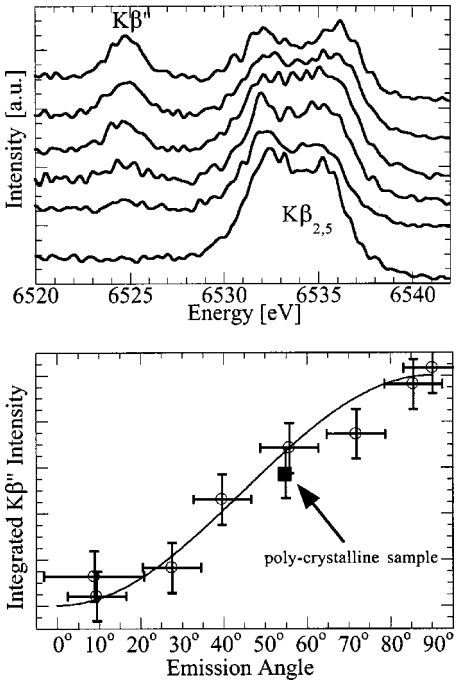

FIG. 3. Top: spectra of single crystalline $[Rh(en)_3][Mn(N)(CN)_5]\cdot H_2O$ recorded at different emission angles. The angles measured between the short Mn–N bond and the direction of the analyzers are (top to bottom): 90°, 72°, 56°, 39°, 26°, 8°. Bottom: Integrated $K\beta''$ intensities after normalization to the main $K\beta$ region and background subtraction. Square represents intensity of polycrystalline sample (see spectrum Fig. 1).

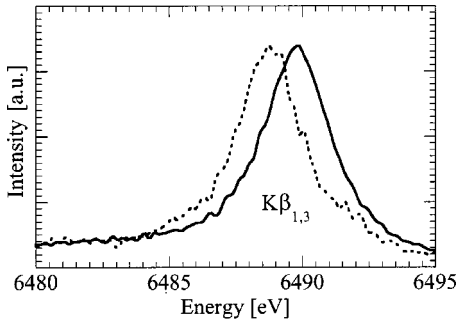

FIG. 4. Anisotropy of the $K\beta_{1,3}$ emission for $[Rh(en)_3][Mn(N)(CN)_5]\cdot H_2O$ crystal. Solid line: emission at 8° to probe $3p_{x,y}$. Dashed line: 90° spectrum minus 0.5 times 8° spectrum to probe $3p_z$. Both spectra are normalized to integrated intensity.

charge density distributions are reported in Table S-1 of the Supplementary Material.[19] In all cases, bond lengths were calculated to better than 0.05 Å. With the ADF program package it is customary to use frozen-core basis sets. However, in order to calculate transitions involving core orbitals it is necessary to employ all-electron basis sets. We therefore verified that only minor differences were observed between the properties calculated using the standard frozen core basis sets and those that were calculated using the all-electron bases.

The $K\beta_{1,3}$ transition energy was calculated to be 6440 or 6422 eV using the Slater transition state method and either LDA or GC functionals, respectively. This is about 1% lower than the measured value of 6490 eV. The calculations predicted a noticeable ligand field splitting of the Mn $3p$ orbitals: 1.3 ± 0.1 eV (Table S-2 Supplementary Material). As shown in Fig. 4, the $K\beta_{1,3}$ peak does in fact shift by ~1.0 eV to lower energies, in good agreement with the calculations. Previously, the largest reported crystal field shift for transition metal core→core emission was 0.8 eV (for V_2O_5).[20–22] As pointed out by Bendix, the 1.49 Å Mn–N distance in our sample is the shortest known metal–ligand multiple bond length.[6] This presumably gives rise to the larger splitting that we observe.

We also calculated the $K\beta''$ transition energy, using either the Slater transition state method or the ΔSCF method, and either LDA or GC functionals (Table I). The $13A_1$ orbital involved in this transition was found to be relatively pure N($2s$) (87.8% and 86.0% in the GC and LDA calculations, respectively). The calculated transition energies were again too low by 50–70 eV. Similar results were noted by Mukoyama, who only considered differences between transition energies.[23] We adopt the same approach for interpretation of valence band features.

There has been discussion in the past about whether the 'crossover' line oscillator strength comes from ligand $2s$–metal $1s$ overlap or whether it derives purely from the small amount of metal p character in the valence orbital.[23] (The 8% metal $3d$ character can only contribute to quadrupole transitions to the $1s$ orbital.) The experimental data clearly show that this feature has a transition dipole oriented along the Mn–N axis. The transition probability W_{if} between initial state i and final state f is proportional to $\omega_{if}^3|\mathbf{r}_{if}|^2\sin^2\theta$, where $|\mathbf{r}_{if}|^2=|\mathbf{x}_{if}|^2+|\mathbf{y}_{if}|^2+|\mathbf{z}_{if}|^2$ is the dipole matrix element between the two states and θ is the angle between the propagation vector of the emitted photon and $\mathbf{r}$.[24] In C_{4v} symmetry with the irreducible representations A_1, A_2, B_1, B_2, and E, (x,y) transform as E and z transforms as A_1. The Mn($1s$) orbital has A_1 symmetry and we therefore only have to consider molecular orbitals with E symmetry for $|\mathbf{x}_{if}|^2$ and $|\mathbf{y}_{if}|^2$ and orbitals with A_1 symmetry for $|\mathbf{z}_{if}|^2$. The observed angular distribution of the $K\beta''$ intensity clearly assigns it to a molecular orbital with A_1 symmetry, since the fluorescence intensity becomes zero when looked along the z direction (corresponding to (x,y) polarization). In Table S-3 of the Supplementary Material the $13A_1$ MO has the expected energy shift from Mn($3p$) (compare also with Table I) and is used in the following to address the question about the origin of the transition intensity.

First we evaluate the dipole matrix elements $\langle \mathrm{Mn}\,1s|(x,y,z)|c_n\phi_n\rangle$, where $c_n\phi_n$ is the nth atomic orbital component of the molecular orbital in the presence of a core hole. The results are summarized in Table S-4 of the Supplementary Material. As expected, a "pure" Mn($4p$) orbital yields the largest overlap integral. However, it is only a factor of 2.7 greater than the values for the $N^{\mathrm{nitrido}}(2s,2p)$ orbitals. Combining this result with the relative contributions to $13A_1$ shows that, in fact, 91.2% of the $K\beta''$ oscillator strengths comes from a $N^{\mathrm{nitrido}}(2s)$ orbital while the Mn($3p$) and Mn($4p$) orbitals only account for 3.1% and 4.7%, respectively. Note that the Mn atom and C^{cis} and N^{cis} atoms are not in a plane giving small but finite values for the *cis*-ligand $2s$ and $2p_{x,y}$ orbitals in $\langle \mathrm{Mn}\,1s|z|c_n\phi_n\rangle$ and for the

TABLE I. Calculated and experimental $K\beta''$ and $K\beta_{1,3}$ energies (eV).

Method	Gradient-corrected			Local density approximation			Experiment		
	$K\beta''$	$K\beta_{1,3}$	Δ	$K\beta''$	$K\beta_{1,3}$	Δ	$K\beta''$	$K\beta_{1,3}$	Δ
Slater TS	6474.5	6439.3	35.2	6456.5	6421.1	34.7	6524.8	6489.5	35.3
ΔSCF				6452.2					

cis-ligand $2p_z$ orbital in $\langle \mathrm{Mn}\,1s|(x,y)|c_n\phi_n\rangle$.

We turn now to the highest energy valence→core transitions, the so-called $K\beta_{2,5}$ region. There are 17 possible transitions in this energy range of which 12 with A_1 or E symmetry are dipole allowed (Table S-3 of the Supplementary Material). Using furthermore the overlap integrals (Table S-4) it is easy to see that the first significant contributions stem from $15A_1$ and $6E$ resulting in an energy band ~8.5 eV above $13A_1$. In addition there are contributions from a group of transitions with energies shifts ranging from 9.9 to 12.3 eV, resulting in a second band peaked at ~10.8 eV above $13A_1$. For comparison two bands at 8 and 10.5 eV (8° spectrum) and 7.5 and 11.3 eV (90° spectrum), respectively, are observed experimentally (Fig. 5). Due to this multitude of transitions with similar energies, a clear separation between E and A_1 is experimentally not possible in the $K\beta_{2,5}$ region. Nevertheless there are trends that can be seen in both experiment and calculation. In (x,y) polarization (corresponding closely to the 8° spectrum) the only contribution to the lower band is from the $6E$ orbital, which is dominated by transitions from Mn$(4p)$ (48%) and $C^{cis}(2s)$ (30%). In (x,z) or (y,z) polarization (90° spectrum) the $6E$ intensity is reduced by 50% but there is an additional transition from $15A_1$, which is dominated by 39% $C^{trans}(2s)$ and 37% Mn$(4p)$. As shown in the stick diagram of Fig. 5, $15A_1$ contributes 28% of the $6E$ intensity. The total intensity of the lower $K\beta_{2,5}$ band should therefore decrease by a factor of ~1.6 when going from (x,y) to (y,z) or (x,z) polarization. A change of a factor 1.7 in observed in the experimental spectra.

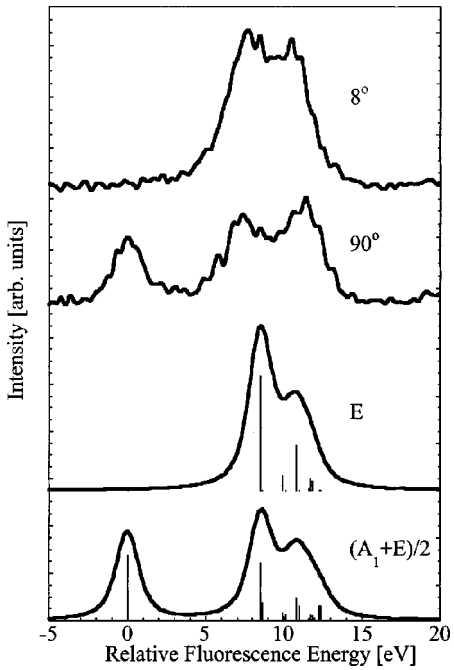

FIG. 5. Simulation of the valence→core emission spectra using DFT calculations compared to the 8° and 90° experimental spectra.

The calculated total intensity of the higher $K\beta_{2,5}$ band changes only slightly with polarization. The loss in intensity from E orbitals is compensated by A_1 contributions. Thus the lower band looses relative to the higher band by changing the emission polarization from (x,y) to (x,z) or (y,z), and a similar trend is observed in our experimental spectra. Finally, in (x,y) polarization the highest calculated fluorescence energy comes from $11E$ at a shift of 11.8 eV compared to the $19A_1$ contribution at 12.3 eV in (x,z) or (y,z) polarization. This results in a 0.5 eV shift of the high energy flank of the $K\beta_{2,5}$ structure. In comparison, the measured spectra show a 1 eV shift.

IV. SUMMARY

The valence→core region of transition metal x-ray spectra contains a wealth of information about the electronic and molecular structure of a system. There is even more information in single crystal spectra. We have been able to interpret these spectra using DFT calculations. The calculations were quite successful at predicting the relative energies of the different transitions. Additional work is needed to better simulate the transition intensities, which depend critically on the electron density near the metal nucleus.

The $K\beta''$ and $K\beta_{2,5}$ features are highly polarized along molecular axes. Angular dependence in $K\beta$ emission has the potential for yielding orientation-dependent EXAFS from powder or solution samples. By monitoring the emission intensity of a fluorescence peak with large anisotropy, one could obtain EXAFS excitation spectra selective for those molecules with transition dipoles perpendicular to the analyzer. Related ''photoselection'' experiments are common in UV–visible,[25] ENDOR,[26] and other spectroscopies. Experiments to assess the feasibility of this approach are in progress.

ACKNOWLEDGMENTS

The authors thank Hal Tompkins and the beamline 10-2 staff at SSRL for assistance in making these experiments possible. This work was supported by the National Institutes of Health Grants No. GM-44380 (S.P.C.), the DOE Office of Biological and Environmental Research (S.P.C.) and the National Science Foundation Grant No. CHE-0078809 (H.B.G.). Portions of this research were carried out at the Stanford Synchrotron Radiation Laboratory, a national user

facility operated by Stanford University on behalf of the U.S. Department of Energy, Office of Basic Energy Sciences.

[1] R. Jenkins, *X-Ray Fluorescence Spectrometry*, 2nd ed. (Wiley–Interscience, New York, 1999).
[2] A. E. Lindh and O. Lundquist, Ark. Mat., Astron. Fys. **18**, 14 (1924).
[3] A. Meisel, G. Leonhardt, and R. Szargan, *X-Ray Spectra and Chemical Binding* (Springer-Verlag, New York, 1989).
[4] U. Bergmann and S. P. Cramer, Proc. SPIE **3448**, 198 (1998).
[5] U. Bergmann, M. M. Grush, C. R. Horne *et al.*, J. Phys. Chem. B **102**, 8350 (1998).
[6] J. Bendix, R. J. Deeth, T. Weyhermüller, E. Bill, and K. Wieghardt, Inorg. Chem. **39**, 930 (2000).
[7] J. Bendix, Ph.D. thesis, University of Copenhagen, 1998.
[8] E. J. Baerends, D. E. Ellis, and P. Ros, Chem. Phys. **2**, 41 (1973).
[9] L. Versluis and T. Ziegler, J. Chem. Phys. **322**, 88 (1988).
[10] G. te Velde and E. J. Baerends, J. Comput. Phys. **99**, 84 (1992).
[11] C. Fonseca Guerra, J. G. Snijders, G. te Velde, and E. J. Baerends, Theor. Chem. Acc. **99**, 391 (1998).
[12] A. D. Becke, Phys. Rev. A **38**, 3098 (1988).
[13] J. P. Perdew, Phys. Rev. B **33**, 8822 (1986).
[14] J. P. Perdew, Phys. Rev. B **34**, 7406 (1986).
[15] R. S. Mulliken, J. Chem. Phys. **23**, 1833 (1955).
[16] J. C. Slater, *Quantum Theory of Molecules and Solids* (McGraw–Hill, New York, 1974).
[17] G. Peng, F. M. F. Degroot, K. Hämäläinen *et al.*, J. Am. Chem. Soc. **116**, 2914 (1994).
[18] U. Bergmann, C. R. Horne, T. J. Collins, and S. P. Cramer, Chem. Phys. Lett. **302**, 119 (1999).
[19] See EPAPS Document No. E-JCPSA6-115-003148 for tables. This document may be retrieved via the EPAPS homepage (http://www.aip.org/pubservs/epaps.html) or from ftp.aip.org in the directory /epaps/. See the EPAPS homepage for more information.
[20] I. B. Borovskii and V. I. Matiskin, Dokl. Akad. Nauk SSSR **192**, 63 (1970).
[21] G. Dräger and O. Brümmer, in *Inner-Shell and X-Ray Physics of Atoms and Solids*, edited by D. J. Fabian, H. Kleinpoppen, and L. M. Watson (Plenum, New York, 1980).
[22] G. Dräger and O. Brümmer, Phys. Status Solidi B **98**, K33 (1980).
[23] T. Mukoyama, K. Taniguchi, and H. Adachi, Phys. Rev. B **41**, 8118 (1990).
[24] H. A. Bethe and E. E. Salpeter, *Quantum Mechanics of One- and Two-Electron Systems* (Springer, Berlin, 1957).
[25] D. S. Kliger, J. W. Lewis, and C. E. Randall, *Polarized Light in Optics and Spectroscopy* (Academic, San Diego, 1990).
[26] J. R. Pilbrow, *Transition Ion Electron Paramagnetic Resonance* (Clarendon, Oxford, 1990).